Modeling the Evolution of Grain Texture during Solidification of Laser-Based Powder Bed Fusion Manufactured Alloy 625 Using a Cellular Automata Finite Element Model

Carl Andersson [ID] **and Andreas Lundbäck** *[ID]

Department of Engineering Sciences and Mathematics, Division of Solid Mechanics,
Luleå University of Technology, 971 87 Luleå, Sweden; carl.andersson@ltu.se
* Correspondence: andreas.lundback@ltu.se

Abstract: The grain texture of the as-printed material evolves during the laser-based powder bed fusion (PBF-LB) process. The resulting mechanical properties are dependent on the obtained grain texture and the properties vary depending on the chosen process parameters such as scan velocity and laser power. A coupled 2D Cellular Automata and Finite Element model (2D CA-FE) is developed to predict the evolution of the grain texture during solidification of the nickel-based superalloy 625 produced by PBF-LB. The FE model predicts the temperature history of the build, and the CA model makes predictions of nucleation and grain growth based on the temperature history. The 2D CA-FE model captures the solidification behavior observed in PBF-LB such as competitive grain growth plus equiaxed and columnar grain growth. Three different nucleation densities for heterogeneous nucleation were studied, 1×10^{11}, 3×10^{11}, and 5×10^{11}. It was found that the nucleation density 3×10^{11} gave the best result compared to existing EBSD data in the literature. With the selected nucleation density, the aspect ratio and grain size distribution of the simulated grain texture also agrees well with the observed textures from EBSD in the literature.

Keywords: additive manufacturing; SLM; microstructure; equiaxed; columnar; CET; numerical; simulation

1. Introduction

Additive manufacturing (AM) is transforming the manufacturing industry by allowing complex-shaped geometries to be manufactured while reducing material waste compared to subtractive methods such as milling [1]. In additive manufacturing, the material is added in a layer-by-layer approach and by subsequently melting the added material with a heat source it is fused into a solid structure [2]. Laser-based powder bed fusion (PBF-LB) is one of the most common additive manufacturing methods where a thin layer of metal powder is first spread and then selectively melted using a laser beam, also known as selective laser melting (SLM) [3]. The nickel-based superalloy 625 is a common AM material and it is widely used in the aerospace, chemical, and petrochemical industries due to its good yield strength, creep strength, and weldability [4], as well as its good oxidation and corrosion resistance [5]. Dendritic columnar and equiaxed microstructures are typically seen in alloy 625 parts produced by PBF-LB [6,7]. These microstructural features arise from dendritic crystal growth. As the crystals grow, grains are forming consisting of dendritic crystals that share the same crystallographic orientation. The grain texture refers to the distribution of these grains and their crystallographic orientations. Each oriented crystal has its preferential growth direction. If the preferential growth direction is aligned with the maximum heat flow direction it is more likely to sustain its growth and outcompete other growing crystals. This is known as competitive grain growth which has a significant influence on the grain textures of PBF-LB produced materials. The maximum heat flow direction in additive manufacturing is along the build direction which causes pronounced columnar grain textures oriented along the build direction as seen in Malmelöv et al. [8].

The mechanical properties of the produced material will vary depending on the obtained grain texture. Through modeling, the desired mechanical properties can be obtained, while costly, time consuming, and material-demanding physical tests can be avoided. To be able to model the grain texture evolution, the solidification process in AM needs to be understood. Figure 1 illustrates the solidification process and the characteristics of the as-solidified grain texture. Additive manufacturing is comparable to many repetitive welds and therefore it is assumed that the nucleation and grain growth mechanisms are similar to those of the welding described by Kou [9]. There are two competing nucleation mechanisms that take place while the melt pool is solidifying: epitaxial nucleation and heterogeneous nucleation. Epitaxial nucleation occurs [10] at the interface between solid material and the end of the solidification zone. Pre-existing crystals that are partially re-melted start to grow into the undercooled liquid to form columnar grains. Heterogeneous nucleation occurs in the undercooled liquid where grains nucleate due to bulk nucleation which forms equiaxed grains. If the equiaxed zone grows large enough, the columnar front will be prevented from growing further and the Columnar-to-Equiaxed Transition (CET) takes place. By varying the process parameters, the equiaxed zone can be more likely to sustain its growth due to more favorable conditions which promotes the CET [11,12].
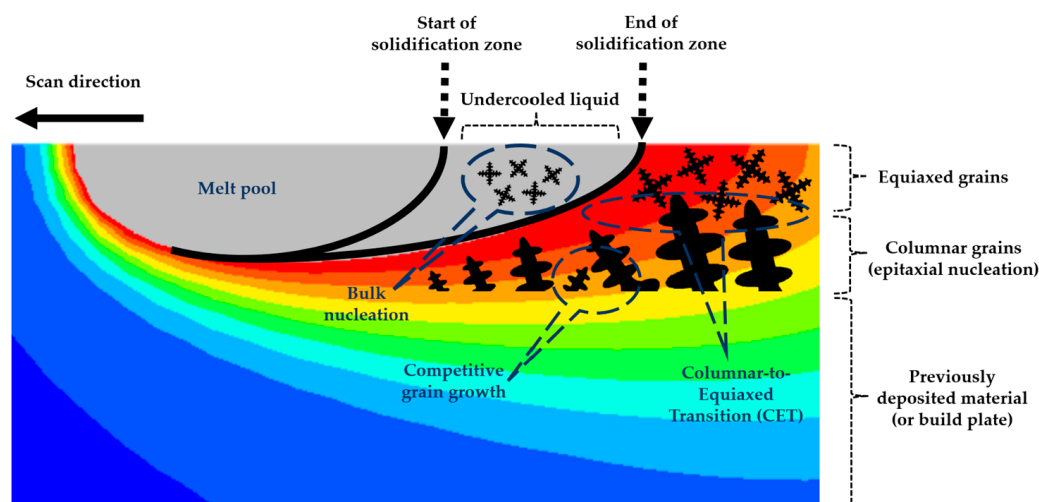

Figure 1. Nucleation and grain growth mechanisms in welding [9] which is assumed to be similar as in additive manufacturing.

There are three common models used to predict the grain texture during solidification: the Phase Field (PF) model, the Cellular-Automata (CA) model, and the Kinetic Monte-Carlo (KMC) model [13,14]. The PF model is used to predict the dendritic growth during solidification, resulting in a high-resolution prediction of the dendritic growth but is thus also limited to predictions containing a few dendrites [15]. The CA model describes the dendritic growth on a cell grid where each cell can exist in different states and the cells evolve between states according to predefined transition rules. The model applies to mesoscale objects since only the growth of the dendrite tip is considered which significantly reduces the computational time compared to the PF model that considers the entire liquid–solid interface of the dendrite. The KMC model is computationally efficient enough to reproduce full 3D microstructures that agrees with experimental findings [16], but it cannot predict grain texture since it does not incorporate the effects of crystallographic orientation and competitive grain growth [13,16]. The CA model was deemed as most suitable to predict the characteristics of the printed grain texture efficiently and accurately in a mesoscale context applied to PBF-LB.

In the 1990s, Gandin and Rappaz developed a CA model to predict the grain texture evolution during solidification of casted parts [12,17,18]. CA models have gained popularity for simulating the grain texture evolution in alloys manufactured by PBF-LB due to the advancements in the field of additive manufacturing. Typically, 2D CA models are

used for their computational efficiency while being capable of simulating realistic grain textures [19,20]. Dezfoli et al. [19] used a 2D CA model to simulate the grain texture from single-track PBF-LB processed alloy 718. A cell spacing of 0.2 μm was used in their CA model when considering the PBF-LB process conditions of 150 W for three different scan velocities of 500, 400, and 300 mm/s. The cell spacing is an important parameter that controls the spatial resolution in the CA model. Rai et al. [20] developed a 2D CA model to predict the grain texture of alloy 718 consisting of 10 layers processed by electron beam powder bed fusion (PBF-EB). The CA model with a cell spacing of 0.5 μm was used to compute the grain texture based on the thermal history obtained with a 2D Lattice Boltzmann model. In their case, the process condition for PBF-EB was a scan velocity of 2200 mm/s and a power of 594 W.

Although 2D models do produce realistic results for AM, they do not capture all aspects of grain growth. For example, the 2D model would not be able to capture the influence on the grain texture when grains are growing out of the plane. Numerous researchers have developed 3D CA models capable of simulating the grain texture evolution that also captures the growth of grains out of the plane [21,22]. Koepf et al. [21] developed a 3D CA-FE model that re-uses the thermal field obtained using a finite element (FE) model with four printed layers. They predicted the grain texture of the nickel-based alloy CMSX-4 produced by PBF-EB. With the re-use of the temperature field, the computational time was significantly reduced. The process conditions included a power of 300 W and a scan velocity of 500 mm/s. A spatial resolution of 10 μm was used to capture the evolution of the grain texture. Teferra and Rowenhorst [22] developed a 3D CA model where parallelization was implemented to increase computational efficiency. The PBF-LB process with a power of 175 W and a scan velocity of 500 mm/s was simulated to study the grain texture evolution of 316 L stainless steel using a spatial resolution of 1.875 μm in the CA model.

First and foremost, in the highlighted findings mentioned above, it is seen that the spatial resolution is lower for 3D models than for 2D models, and thus the accuracy of a 3D model is inherently lower. Hence, there is a need for 2D CA models that can be used both with a fine spatial and temporal resolution while also giving a reasonable computational time. In 2D CA modeling, the two competing nucleation mechanisms have a significant influence on the predicted grain texture. One of these is, as mentioned earlier, heterogeneous nucleation, and the choice of nucleation parameters are essential for success in grain texture modeling as highlighted in the review by Körner et al. [13]. The importance of choosing nucleation parameters for 2D CA models is often neglected such that nucleation density and heterogeneous nucleation are not considered. In this work, a method of finding suitable nucleation parameters for heterogeneous nucleation is proposed by calibrating them with respect to existing EBSD data in the literature. Secondly, the largest contribution to the computational time is from the thermal model. Therefore, there is a need for efficient 3D FE models that can resolve the temperature history for complex scan strategies seen in PBF-LB. In this work, a 3D FE heat transfer model is developed capable of simulating the temperature history over many deposited layers. Thermal models coupled with fluid flow such as in Dezfoli et al. [19] are used in conjunction with models for grain texture evolution. These models have the possibility to give a high resolution of the temperature field but with the price of a high computational cost. Typically, 2D Lattice Boltzmann methods are also used coupled with particle interactions such as in Rai et al. [20]. However, since heat transfer is a 3D phenomenon, the accuracy of the temperature history from such a model will be inherently lower and it cannot resolve the temperature history involving rotation scanning strategies which are often used in PBF-LB.

The aim of this work is to develop an efficient 2D CA-FE model that can predict the grain texture of the nickel-based superalloy 625 processed by PBF-LB. Both heterogeneous nucleation and epitaxial nucleation are considered in the model. Such a model can be used to obtain a better understanding of how the grain texture of the printed material is influenced by the many process parameters in PBF-LB. The prediction is based on the temperature history obtained with a 3D FE heat transfer model for a set of process

parameters from the work by Malmelöv et al. [8]. The heat transfer model combined with a 2D CA model is proposed to efficiently compute grain growth and nucleation in alloys produced by PBF-LB. This enables an efficient modeling approach capable of predicting the grain texture in PBF-LB which evolves over many deposited layers. Nucleation parameters are determined through calibration with regard to existing EBSD data in the literature. The PBF-LB process conditions are then changed relative to the calibration case for model validation to see if the model captures changes in the grain texture depending on the process conditions.

2. Materials and Methods

This section describes the coupled CA-FE model for simulating the grain texture of PBF-LB processed alloy 625. The coupling between the CA and FE model is a one-way coupling. The temperature field is first computed with the FE model and the grain texture is computed as a post-process procedure after all timesteps are computed in the FE model. The finite element model is simulated in MSC Marc with in-house developed AM subroutines and the temperature history is imported into MATLAB where the computations of the CA model are made. The grain texture is computed from a two-dimensional cross section based on the thermal history obtained from the finite element model.

2.1. Finite Element Model

The finite element model was developed to take into account the process conditions for PBF-LB processed alloy 625 as presented in Malmelöv et al. [8]. A wall geometry (length 60 mm, width 4 mm, and height 30 mm) was built in their work and the thermal history for a small part of that build is simulated here (total hatch width 540 μm, scan length 300 μm, total build height 200 μm). The FE model consists of 15 deposited layers with a layer thickness of 20 μm where each layer consists of 9 hatches with the hatch spacing 60 μm and hatch length 300 μm. The scanning strategy was bi-directional and the elements were activated according to the "inactive" element approach. Figure 2 illustrates the multi-layer deposition model composed of the finite element discretization of all deposited layers and the build plate.
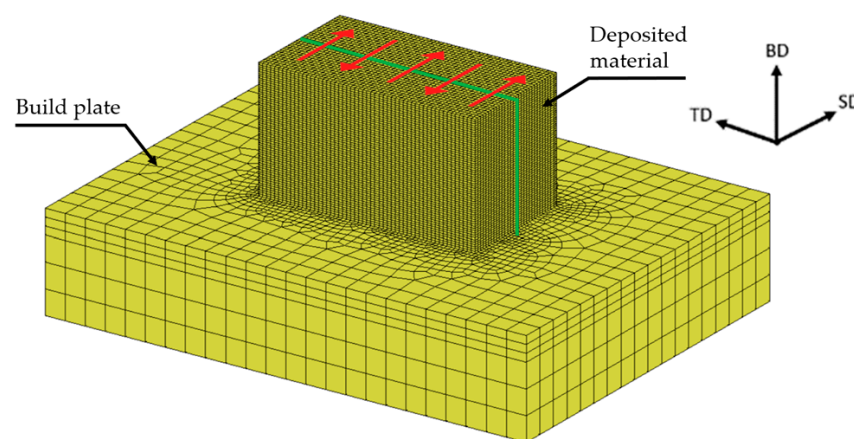

Figure 2. Finite element discretization of the deposited material and substrate where the grain texture is predicted with the CA model in the cross-section in the middle of the deposited layers (green lines). The red arrows indicate the bi-directional scanning strategy.

The discretization of the added layers consists of hexagonal elements with a height of 5 μm which means that one layer consists of four elements in the build direction. In between the added hatches and layers there is a short time of cooling to take a real-life scenario into account. Cooling between hatches was set to the total width of the printed wall divided by the scanning velocity. Cooling between layers was set to the total number of hatches of the printed wall multiplied by the time for cooling between hatches plus additional time for powder recoating. The grain texture is modelled on the BD-TD plane

(build direction, transverse direction) indicated by the green lines in the figure. Two different process parameters are considered, case A and case B, where the power and scan velocity changes. Case A is used for model calibration and case B is used for model validation of the simulated grain texture.

The temperature history is computed from the finite element model by solving the heat conduction equation,

$$\frac{\partial}{\partial x}\left(k\frac{\partial T}{\partial x}\right) + \frac{\partial}{\partial y}\left(k\frac{\partial T}{\partial y}\right) + \frac{\partial}{\partial z}\left(k\frac{\partial T}{\partial z}\right) + \dot{q} = \rho c_p \frac{\partial T}{\partial t} \tag{1}$$

where T is the temperature, $\dot{q}$ is the internal heat generation, ρ is the density, and t is the time. The heat conductivity k and specific heat c_p is given as a function of the temperature as shown in Figure 3.
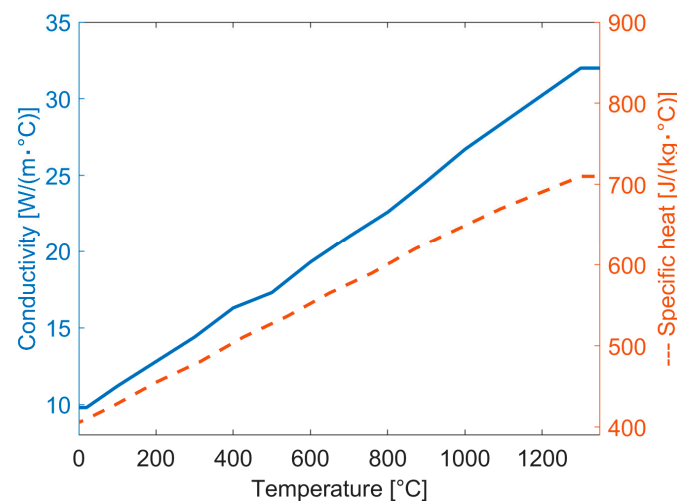

Figure 3. Conductivity [23] and specific heat [24] for alloy 625.

The initial condition is applied as,

$$T(x, y, z, 0) = T_0 \tag{2}$$

where T_0 is the ambient temperature, and the boundary conditions for a free surface are applied as,

$$k\frac{\partial T}{\partial n} - q_s + h(T - T_0) + \sigma\varepsilon(T^4 - T_0^4) = 0 \tag{3}$$

where $\frac{\partial T}{\partial n}$ is the temperature change with respect to the normal direction of the surface and q_s is the external heat flux. $h(T - T_0)$ is heat flow from convection where h is the heat transfer coefficient. The term $\sigma\varepsilon(T^4 - T_0^4)$ gives the heat dissipation from radiation where σ is Stefan-Boltzmann's constant and ε is the emissivity. Dissipation of heat through convection and radiation is considered during deposition and cooling between layers on the top surfaces with the emissivity and convective heat transfer coefficient set to 0.28 and 18 W/(m²·K), respectively [25]. After cooling between layers, recoating occurs and another powder layer is spread onto the deposited layer. During this time, the convection and radiation is inactivated in the model. This is motivated by the fact that the conductivity of the powder is considerably much lower than that of the solidified material [26]. A heat flux film of 500 W/(m²·K) is applied as a boundary condition to the bottom and the sides of the build plate to represent the heat that is conducted to the remaining parts of the build plate and to the fixture of the build plate [8]. Latent heat was set to 150 kJ/kg in the interval 1189–1336 °C for both solidification and melting [27]. The latent heat is released as a linear function between the liquidus and solidus temperature.

Goldak's double ellipsoid heat input model [28] is used to replace the physics of the generation of heat and to mimic the heat input from the laser beam. This model applies a heat flux to all integration points inside of the ellipsoidal geometry which can be described by the following equation,

$$q_{f,r}(x, y, z, t) = \frac{\beta 6\sqrt{3} f_{f,r} Q}{abc_{f,r} \pi \sqrt{\pi}} e^{\frac{-3x^2}{a^2}} e^{\frac{-3y^2}{b^2}} e^{\frac{-3(z+v(\tau-t))^2}{c_{f,r}^2}} \tag{4}$$

where Q is the power input, v is the velocity of the heat source, t is the time, β is a scale factor, τ defines the position of the heat source at $t = 0$, and $f_{f,r}$ defines the fraction of heat deposited in the forward or rear region. The subscripts f and r denotes the forward and rear part of the ellipsoid. The lengths a, b, and c are half of the width, depth, and length of the ellipsoid. The net input power Q is given by,

$$Q = \eta Q_{nom} \tag{5}$$

where Q_{nom} is the nominal heat input and η is the efficiency factor accounting for losses such as reflection and spattering. Table 1 gives a summary of the parameters used in the finite element model. The heat source parameters were chosen based on previous experience and it was ensured that the entire added layer was melted and that the previous deposited layers and hatches were partially remelted.

Table 1. Parameters in the finite element model.

Property	Value	Unit
Power input Q_A [8]	100	W
Scan velocity v_A [8]	1200	mm/s
Power input Q_B [8]	160	W
Scan velocity v_B [8]	1400	mm/s
Heat source efficiency factor η	0.34	-
Half width of heat source a	35	μm
Depth of heat source b	20	μm
Forward length of heat source c_f	15	μm
Rear length of heat input source c_r	25	μm
Initial and ambient temperature T_0	500	°C
Density ρ [24]	8440	kg/m^3

To ensure that the correct amount of heat input is added to the model in each timestep, the scale factor β is added to Equation (4). This scale factor has two parts that it compensates for. The first part is related to the 5% cut-off limit that was proposed by Goldak et al. [28]. This cut-off limit is such that if the volumetric heat flux is below 5% of the peak value it is set to zero. In Lindgren [29], an analytical integration of the heat source equation with the given boundary conditions shows that only 89% of the power is supplied into the model. The second part is related to the loss of heat input due to the discretization. A coarser mesh will generally give a larger loss from the numerical integration of the heat source equation. This loss will vary between each time step depending on the element length in the welding direction, the velocity, and the time step length. The scale factor β is added to Equation (4) to compensate for the heat loss. The scale factor is computed as the ratio between the wanted heat input over the actual heat input. Since the second part of the heat input loss varies in a non-predictive way, it must be computed in each time step. In the current approach, it is conducted such that the scale factor from the previous time step is used as a first guess in the first iteration of the current time step. The scale factor is then computed and applied in the subsequent iteration. Principally, the change in the scale factor can perturbate the solution between the first and second iterations. However, in practice it has been seen that there is little to no increase in the total number of iterations when solving an AM model using this approach.

2.2. 2D Cellular Automata Model

The cellular automata model is based on the framework developed by Gandin and Rappaz [12,17,18] and is described in this section. The temperature history is imported from the finite element model into MATLAB and a linear interpolation to the CA cell grid is made. A finer grid was used for the CA model because it is not as computationally expensive as the FE model. The CA grid contains cells with the spacing l between cells and the spacing between cells was set to 0.5 μm compared to the 5 μm element size in the FE model. The temporal resolution is also refined in the CA model according to,

$$\partial t_{CA} = 0.25 \cdot \frac{l}{\max(v(\Delta T))} \tag{6}$$

where $v(\Delta T)$ is the growth velocity of the dendrite tip as a function of the undercooling. This adaptive timestep algorithm ensures that the dendritic network does not grow more than a quarter of the cell spacing in a single timestep.

Each cell in the grid has its own defined neighborhood and the cell can exist in a solid, nucleated, growing, or liquid state. The neighborhood controls the transition between the states and a Moore's second-order neighborhood with 24 neighbors was used. The cell is said to be liquid when its temperature T is higher than the liquidus temperature T_L and the nucleation of a liquid cell is controlled by its undercooling ΔT defined as the change in temperature below the liquidus temperature. From the liquid phase, a cell can be nucleated into the growing phase and the growth is computed according to a modified version of the decentered square growth algorithm developed by Gandin and Rappaz [17]. The cell becomes solid when the temperature is below the solidus temperature T_S.

2.2.1. Nucleation

Additive manufacturing has many similarities to welding and it is assumed that the nucleation mechanisms are similar to those of welding. Kou [9] notes that one of the main types of nucleation in welding is epitaxial nucleation where pre-existing grains at the fusion boundary are partially remelted which reactivates the grain growth without altering the crystallographic orientation. This type of nucleation is considered in the model. Non-epitaxial growth at the fusion boundary is not considered since this is an effect when two different materials (or different crystal structures) are joined together. This is an important nucleation mechanism for aluminum alloys, and it was considered in the CA model by Mohebbi and Ploshikhin [30]. In this model, both the substrate and the deposited material are alloy 625 where epitaxial growth largely influences the grain evolution in PBF-LB [7] and non-epitaxial nucleation at the fusion boundary is neglected. New grains can also form from the nucleus caused by dendrite fragmentation, grain detachment, surface nucleation, and heterogeneous nucleation [9]. Dendrite fragmentation and grain detachment occur when convection carries detached dendrite fragments or partially detached grains into the weld pool which forms new nuclei. Surface nucleation can occur when a stream of cooling gas causes undercooling on the surface inducing nucleation effects. The effect of these three types of nucleation is neglected in the model since they are assumed to be limited in the protected environment in PBF-LB. It is also indirectly accounted for in the fourth mechanism where new nuclei originate from heterogeneous nucleation on foreign particles in the liquid melt pool.

Heterogeneous nucleation is accounted for in the model in a similar way as proposed by Gandin and Rappaz [12,18]. In their work, the nucleation was treated by heterogeneous nucleation from surfaces or through bulk nucleation in the undercooled liquid. They added the surface nucleation phenomena to capture nucleation sites on the mold walls where nuclei more easily can form due to impurities in the wall. This is not necessary for AM simulations due to the lack of surfaces such as mold walls. Heterogeneous bulk nucleation is dealt with by introducing a nucleation density parameter $n(\Delta T)$ that describes

the number of nucleation sites per cubic volume. The total number of nucleation sites is then given as,

$$N_{max} = n_{max} V \tag{7}$$

where V is the volume of the undercooled liquid. The rate of change for the nucleation density is given by a Gaussian distribution, hence, we can formulate the nucleation density as a function of the undercooling with the integral of the Gaussian probability density function,

$$n(\Delta T) = \int_0^{\Delta T} \frac{dn(\Delta T)}{d(\Delta T)} d(\Delta T) = \frac{n_{max}}{\Delta T_\sigma \sqrt{2\pi}} \int_0^{\Delta T} \exp\left(-\frac{1}{2}\frac{(\Delta T - \Delta T_{avg})^2}{(\Delta T_\sigma)^2}\right) d(\Delta T) \tag{8}$$

where ΔT_{avg} is the average undercooling and ΔT_σ is the standard deviation for the Gaussian distribution, respectively.

Bulk and surface nucleation is sufficient for simulating the solidification of casted parts. For additive manufacturing or any other welding procedure, the epitaxial grain growth must be considered which occurs at the fusion boundary. The nucleation for epitaxial growth is treated in a similar way as the heterogeneous nucleation by re-activating the growth of solid cells according to a Gaussian distribution at high undercooling and at temperatures near the solidus temperature. Figure 4 schematically illustrates the concept of heterogeneous nucleation for bulk nucleation and epitaxial growth. The increase in nucleation sites with respect to the undercooling is given by the blue curve, whereas the red curves describe the total number of available nucleation sites.
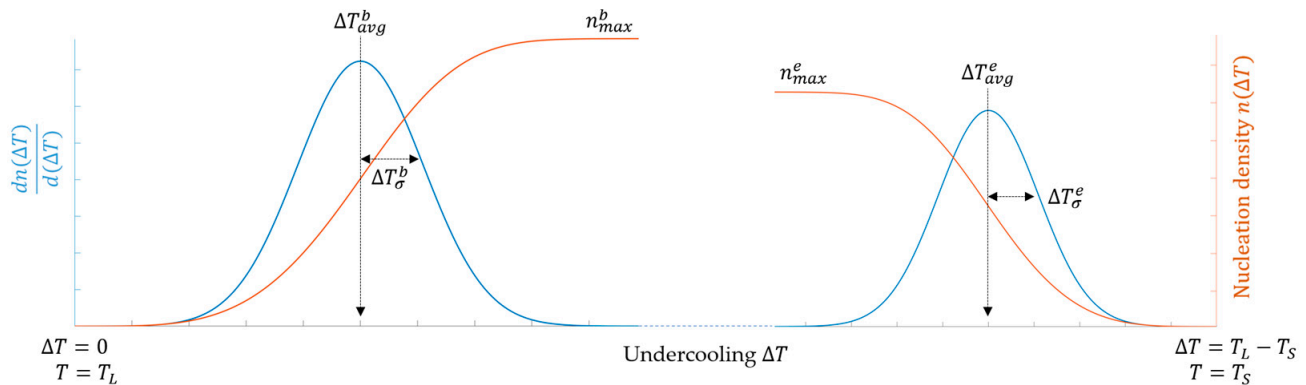

Figure 4. Heterogeneous bulk nucleation. The upper subscript b describes bulk nucleation, while the upper subscript e describes epitaxial growth.

In the CA model, the heterogeneous nucleation is treated by first computing the total number of nucleation sites according to Equation (7). The cross-section area is used instead of the volume for 2D CA models for a given maximum nucleation density. With the number of nuclei known, random cells are chosen and selected as nucleation sites. Each selected cell is appointed a critical undercooling ΔT_{crit}, randomly chosen from the Gaussian distribution with the average ΔT_{avg} and the standard deviation ΔT_σ. When the critical undercooling is exceeded, the nominated cell nucleates, and the cell is assigned a crystallographic orientation. Figure 5 illustrates the concept of heterogeneous nucleation implemented in a cellular automata application. All cells are nominated for epitaxial nucleation, and the reactivation of the growth occurs when the temperature is above the solidus temperature plus the contribution from the Gaussian distribution. The average of the distribution for the epitaxial nucleation was chosen such that the undercooling from the average to the solidus temperature is the same as the undercooling from the average of the heterogeneous nucleation distribution to the liquidus temperature. The standard deviation for the distribution was kept the same for both distributions. A summary of the nucleation parameters is given in Table 2.
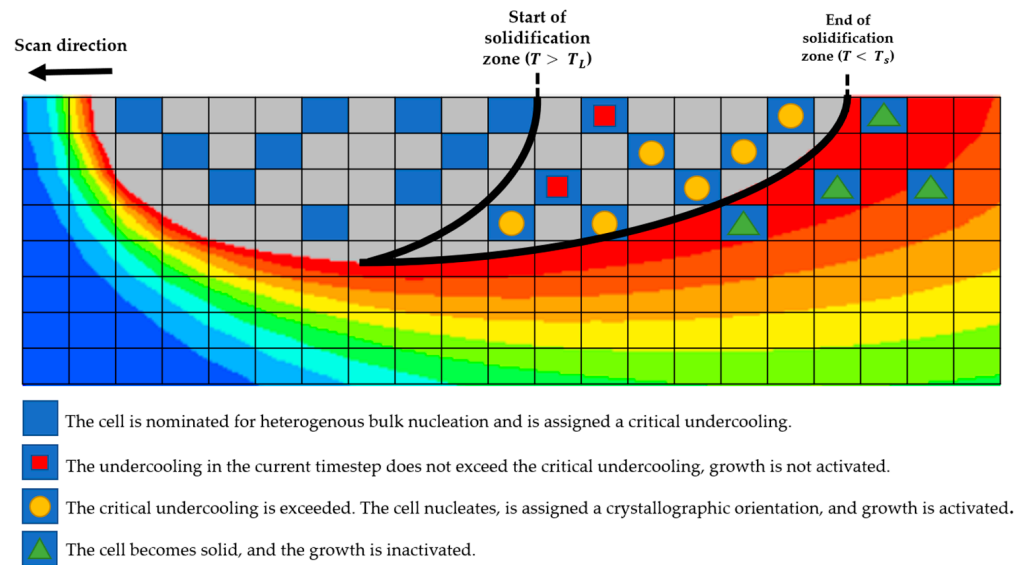
Figure 5. Heterogeneous nucleation in the CA model.

Table 2. Nucleation parameters in the CA model.

Property	Value [°C]
Average bulk nucleation temperature ΔT_{avg}^b [18]	5.5
Standard deviation bulk nucleation ΔT_{σ}^b [12]	0.1
Average epitaxial nucleation temperature ΔT_{avg}^e	141.5
Standard deviation epitaxial nucleation ΔT_{σ}^e	0.1
Liquidus temperature T_L [8]	1336
Solidus temperature T_S [8]	1189

2.2.2. Grain Growth

After nucleation, the cell is given a random crystallographic orientation θ represented by a random integer between 0 and 45 degrees. As a cell has been nucleated, it is allowed to grow. Cells with a temperature between the liquidus and the solidus temperature in the mushy zone are said to be growing. In the growing phase, the dendrite tips grow with the velocity $v(\Delta T)$. The dendrite tip velocity can analytically be computed with the Lipton-Glicksman-Kurz (LGK) model [31] and the Kurz-Giovanola-Trivedi (KGT) model [32]. A simplified expression of the LGK model is commonly used for CA models [22,33,34] which also is used in this work. This expression relates the growth velocity of the dendrite tip as a function of the undercooling as,

$$v(\Delta T) = \frac{D_L}{5.51\pi^2(-m_L(1-k))^{1.5}\Gamma}\left(\frac{\Delta T^{2.5}}{C_0^{1.5}}\right) \tag{9}$$

where D_L is the diffusion coefficient in liquid, m_L is the liquidus slope, k is the partition coefficient, Γ is the Gibbs-Thomson coefficient, and C_0 is the initial concentration. A polynomial function was fitted to this model to further simplify the calculations,

$$v(\Delta T) = a_1\Delta T + a_2\Delta T^2 + a_3\Delta T^3 \tag{10}$$

where a_1, a_2, and a_3 are the polynomial coefficients. The values for the growth kinetic parameters are listed in Table 3 together with the polynomial coefficients. The growth kinetic parameters are taken for a binary approximation of a nickel-based superalloy, and it is assumed that most nickel-based superalloys share similar growth kinetics.

Table 3. Growth kinetics parameters for a binary approximation of a nickel-based superalloy.

Property	Value	Unit
Diffusion coefficient D_L [35]	3×10^{-9}	m^2/s
Liquidus slope m_L [35]	-10.9	K/wt%
Partition coefficient k [35]	0.48	-
Gibbs $-$ Thomson coefficient Γ [35]	10^{-7}	K·m
Initial concentration C_0 [35]	4.85	wt%
1st polynomial coefficient a_1	-4.6×10^{-4}	-
2nd polynomial coefficient a_2	2.80×10^{-5}	-
3rd polynomial coefficient a_3	1.46×10^{-7}	-

In the growing stage, each cell is represented by its growing square oriented with the crystallographic orientation θ where the corners of the square represent the primary dendritic tips that grow according to Equation (10). The square envelope is visualized in Figure 6 and half of the square's side can be computed as follows:

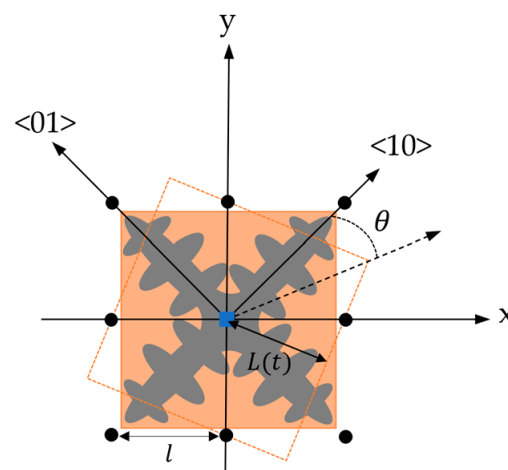$$L(t) = \frac{1}{\sqrt{2}} \int v(\Delta T) \, dt \tag{11}$$

Figure 6. Square envelope of the growing central cell marked by a blue square and its first eight neighbors marked with black dots. The dashed square represents a cell with the crystallographic orientation θ. The corners of the solid square represent the dendritic tip of a crystal misoriented by $\theta = 0$ degrees with the preferential growth vectors <10> and <01>.

The growing central cell is said to capture its neighbors when the neighboring cells are located on or inside the square envelope of the growing central cell. When the neighboring cells are captured, the captured cells inherit the crystallographic orientation θ from the central cell, and new square envelopes are initialized at each of the captured cells with the inherited orientation. The growth center of the newly captured squares is decentered from their local cell position and a virtual growth center of these cells is set at the nearest dendrite tip of the central cell, represented by the corner of the square. The cell grows according to its local undercooling and not with the undercooling at the virtual growth center. This is a similar growth algorithm as the decentered square algorithm proposed by Gandin and Rappaz [17]. It is a somewhat simplified approach since the virtual growth center is directly chosen at the nearest corner with no initial size. More importantly, this method still maintains the dendrite growth front since during the growth of the central cell, the four nearest neighbors are captured first, meaning that these captured cells will have grown to some arbitrary size before the next four nearest neighbors are captured. The size of a square is truncated to a maximum value of $\sqrt{2} \cdot l$ to allow newly initialized squares to grow to an arbitrary size before the growth of the central cell is stopped.

The growth algorithm is illustrated in Figure 7, showing how the square envelopes evolve over several growth steps. Figure 7a shows the growth of the square envelope of a single central cell (red square), having reached a size big enough to capture its four nearest neighbors. New squares are initialized on captured cells but decentered from the center of the captured cells, and the initialized squares are positioned to coincide with the nearest vertex of the cell it was captured by. The central cell and the newly initialized cells continue to grow, reaching the stage in Figure 7b where four additional cells are captured by the central cell. Four new squares are then initialized decentered from their origin and placed on one of the vertices of the central square. After this stage, the complete surrounding of the central cell has been captured and the growth of the central cell is stopped to prevent it from capturing cells that would have been captured by other cells. In the next stage, Figure 7c, the newly initialized envelopes have grown and consequently captured one of its nearest neighbors which is incorporated into the grain. A summary of the transition rules is given in Table 4.
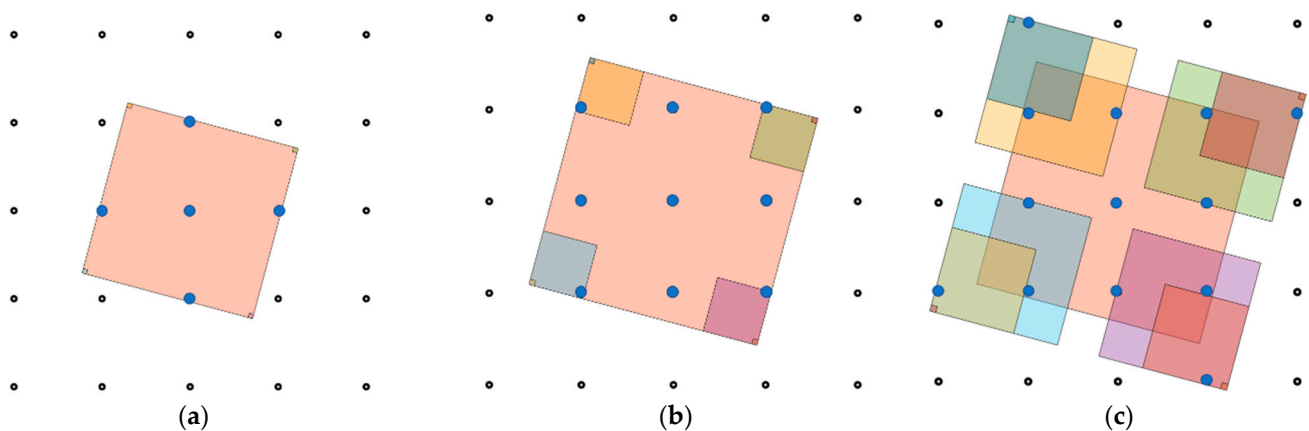

(**a**)　　　　　　　　　　　　　　(**b**)　　　　　　　　　　　　　　(**c**)

Figure 7. Growth over several stages for a single grain with a 15° misorientation consisting of (**a**) four cells, (**b**) nine cells, and (**c**) thirteen cells. The blue solid circles indicate the cells incorporated in the grain at each growth stage, and black hollow circles are the remaining liquid cells in the neighborhood.

Table 4. Summary of transformation conditions between states in the CA model.

Cell State	Condition	Effect in CA Model
Liquid	Temperature T above the liquidus temperature T_L.	The cell does not grow and can be captured by other cells. If the cell is nominated for nucleation, the cell is assigned a critical undercooling ΔT_{crit} that must be exceeded for a nucleus to form.
Nucleated	Undercooling ΔT above the assigned critical undercooling ΔT_{crit}.	The cell can grow and is assigned a random crystallographic orientation θ.
Growing	Temperature above solidus temperature T_S and below the liquidus temperature T_L.	The growth of the cell's square size $L(t)$ is computed according to Equations (10) and (11). The cell can capture cells without a crystallographic orientation θ, and the cell transfers the crystallographic orientation θ to captured cells
Solid	Temperature T below the solidus temperature T_S.	The cell has a crystallographic orientation θ, does not grow, and cannot be captured by other cells.

3. Results and Discussion

In the results and discussion section, the characteristics of the simulated grain texture are first discussed. The influence of the number of nucleation sites on the grain texture is then studied and the simulated grain texture from case A is compared to existing EBSD imaging in the literature to determine a suitable nucleation density. The simulated grain texture is then compared to case B where the process conditions for PBF-LB are changed.

3.1. Characteristics of the As-Solidified Grain Texture

Figure 8 illustrates the characteristics of the as-solidified grain texture where some features are highlighted and discussed. The grain texture of the build plate was first initialized by heterogeneous nucleation during uniform cooling, giving the equiaxed zone at the bottom of the figure. The 15 layers of materials were then deposited. The melt pool geometry during deposition is outlined in the figure. In the outlined melt pool geometry, it is seen that the coarse grains form in the overlapping of the melt pools. This was also seen by Andreau et al. [10] in EBSD imaging where the melt pool geometry was also computed. They reported on the finding that columnar grains grow in the overlapping of adjacent melt pools which is also seen in this case. Phase-field simulations coupled with a thermal-fluid model have also confirmed this grain growth behavior in the work by Yang et al. [36] where they saw coarse grains in the overlapping zone and elongated grains in the center of the melt pool. It is seen in Figure 8 that the elongated grains with a high aspect ratio also coincide with the center of the melt pools. It is seen that these elongated grains tend to grow from the overlapping to the center of the melt pools, creating a boundary between larger columnar grains. It is also seen that when the growth of grains is suppressed, the grains tend to obtain a V-shaped form. This was previously seen in EBSD imaging by Wang et al. [37] where they discussed that the V-shaped grain starts at the overlap between two adjacent melt pools in a lower layer and ends at the overlap between two adjacent melt pools in an upper layer.
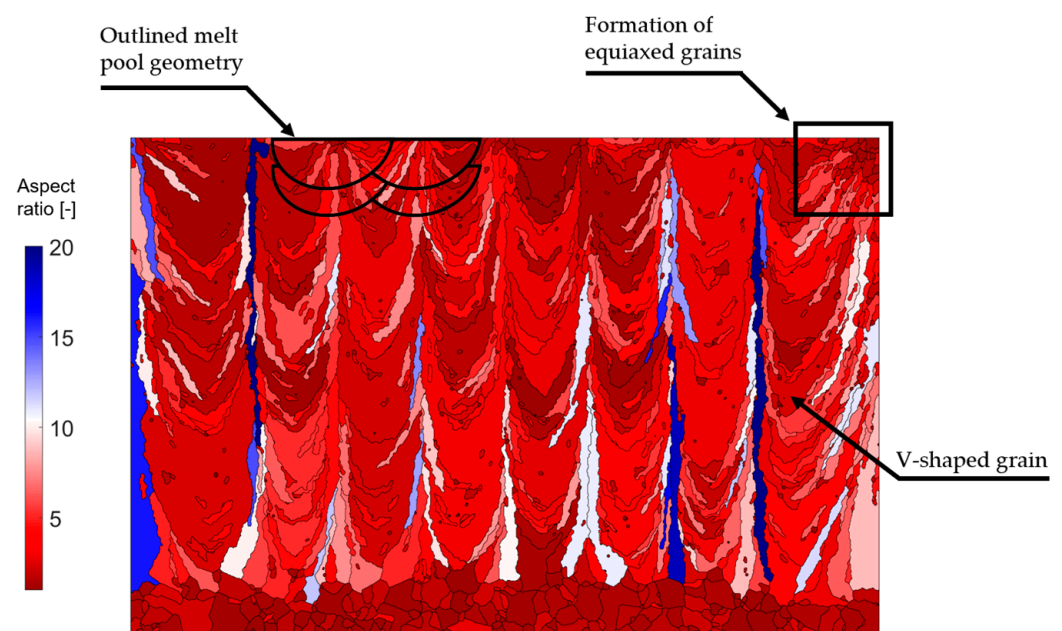

Figure 8. Aspect-ratio of the computed grain structure using 5×10^{11} nucleation density. Some characteristics of the as-solidified grain texture are highlighted.

A zone of equiaxed grains is formed at the top-right of Figure 8. This is not credited to the choice of process parameters. It is rather because it is the last deposited hatch, see Figure 9c, where the cooling conditions and melt pool geometry changes in the FE model compared to the other hatches (hatches 2–8), see Figure 9b. For the last deposited hatch, the cooling conditions give more favorable conditions for equiaxed grains to grow. The first hatch also has different cooling conditions but equiaxed grains are not forming, see Figure 9a. It is also seen that both the first and the last hatch become wider than the intermediate hatches.
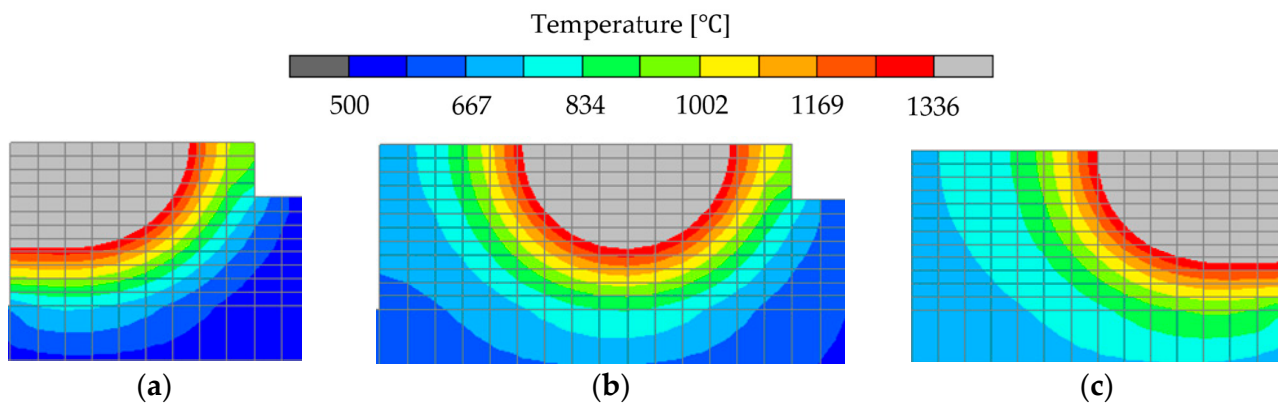
Figure 9. Three scenarios during deposition of hatches for the third layer giving different temperature gradients and rates on the studied BD-TD plane, (**a**) shows the first added hatch on the layer, (**b**) is the intermediate hatches, and (**c**) is the last added hatch on the layer. The gray zone shows the geometry of the melt pool.

3.2. Influence on Grain Texture by Nucleation Density

Figure 10 shows different types of simulated grain textures obtained when using different nucleation densities n_{max}. The top three layers of an already simulated texture were used as an initial substrate rather than having an equiaxed build plate as shown in Figure 8. This is because the simulation should represent a volume somewhere in the middle of the wall to be comparable with experiments from Malmelöv et al. [8]. It should be noted that the color fringe is difficult to compare between simulation and experiments since in the 2D model there is only one Euler angle giving the rotation of the crystal while in 3D three Euler angles give the rotation of the crystal. Instead, the general trend of the epitaxial grain growth is discussed rather than the trends of the crystallographic orientation. The calibration is referred to as case A where the scanning velocity was set to 1200 mm/s and the power was set to 100 W.

In Figure 10a, most of the grains grow epitaxially through all the 15 deposited layers when using a nucleation density of 1×10^{11}. Figure 10b shows a texture with most of the grains growing epitaxially through at least five of the deposited layers when using a nucleation density of 3×10^{11}. The texture for the nucleation density 5×10^{11} in Figure 10c shows how the grain texture consists mostly of grains that do not grow epitaxially through five or more deposited layers. Even less epitaxial growth is observed for the nucleation density 10×10^{11} in Figure 10d. These results show the significance of using the right nucleation density since the grain texture is largely influenced by this number, and thus this value must be calibrated to experimental observations. By visual comparison to the EBSD imaging from Malmelöv et al. [8], it is seen that 1×10^{11} is too low for a nucleation density since no grain grew epitaxially through 15 layers in the experiment. The nucleation density 10×10^{11} is too high since there were grains that grew epitaxially over more than five layers.

When comparing the trends of the crystallographic orientation in the simulated textures, it is seen for a nucleation density of 10×10^{11} in Figure 10d that most larger grains have an orientation of 30 degrees or more. Grains that have a high misalignment of dendrite tip with the heat flow direction tend to become crowded out by the grains with more favorable orientations. These unfavorably oriented grains tend to be small and slender with a crystallographic orientation between 0 and 10 degrees. This shows that the competitiveness of grain growth is captured by the model. This trend is to some extent captured by the lower nucleation densities of 3×10^{11} and 5×10^{11}, however, there are some larger grains with a high misalignment of the dendritic tip.
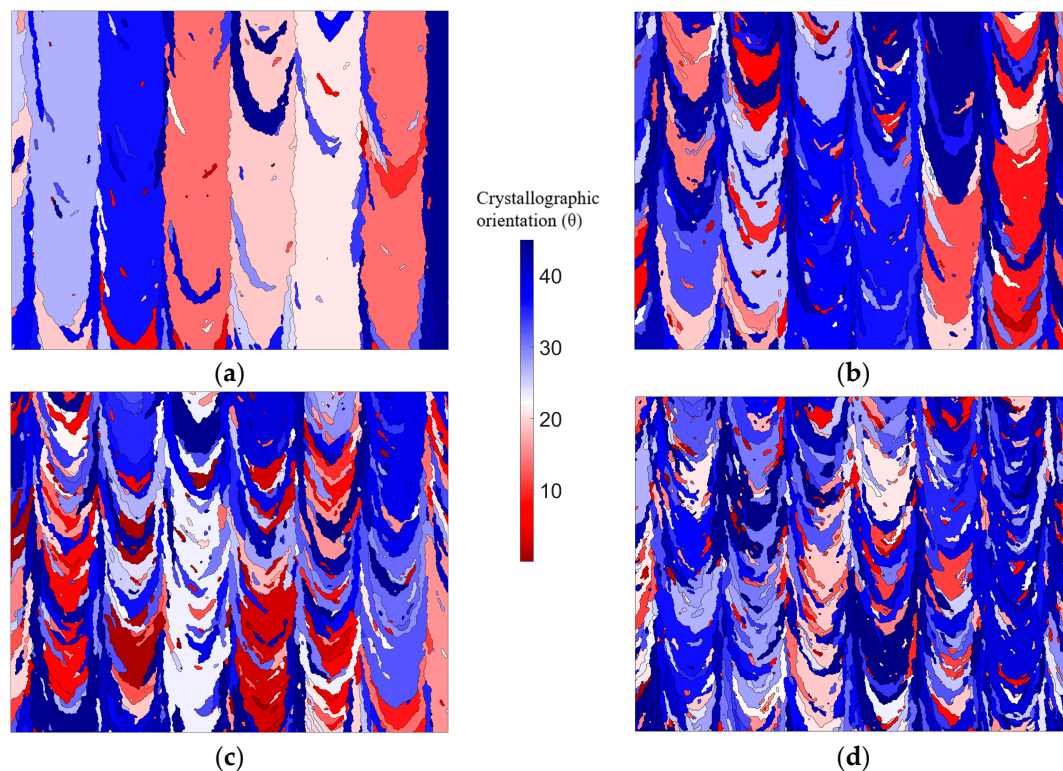
Figure 10. Simulated grain texture for different nucleation densities n_{max} (**a**) 1×10^{11}, (**b**) 3×10^{11}, (**c**) 5×10^{11}, and (**d**) 10×10^{11}.

The aspect ratio was plotted versus the grain size in Figure 11a for three of the simulated grain textures, neglecting the texture for nucleation density 10×10^{11} which contains too many small grains compared to the EBSD imaging from Malmelöv et al. [8]. The analysis was made using the MATLAB toolbox MTEX and only grains that contained 200 or more pixels were considered like the analysis in Malmelöv et al. [8]. It is seen that for all simulations most grains are smaller than 1500 $(\mu m)^2$ with an aspect ratio below 10 which agrees with the measurements.
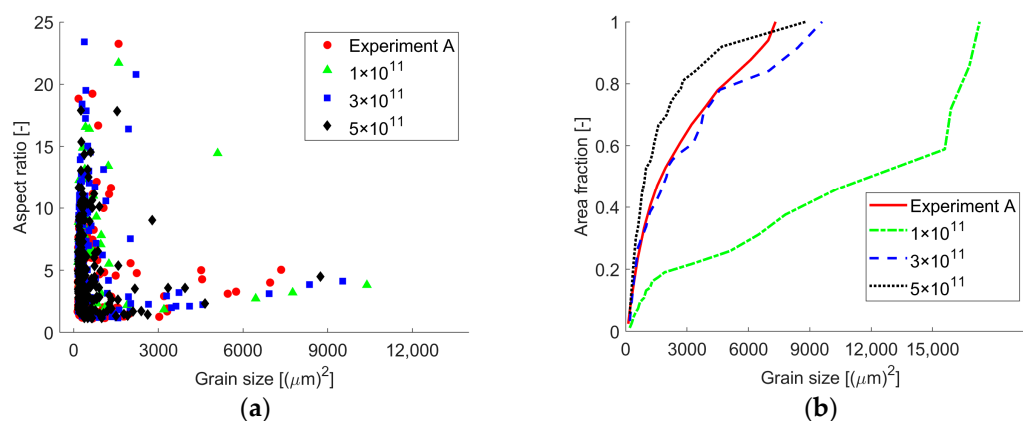

Figure 11. Comparison between simulated grain texture for different nucleation densities with experimental data adapted from Reference [8] where (**a**) shows the aspect ratio vs. grain size dot plot and (**b**) shows the grains' accumulated contribution to the total analyzed area.

The grain size distribution for grains smaller than 2000 $(\mu m)^2$ is illustrated in Figure 12. The grain texture with the nucleation density 1×10^{11} predicts grain sizes that are too large compared to the measured values, see Figure 12a. For the nucleation density of 5×10^{11}, most of the grains are smaller than those of the experiments, see Figure 12c. The

nucleation density 3×10^{11} also predicts too small grains although to a much lesser extent than nucleation density 5×10^{11}. When comparing the grains' accumulated contribution to the total analyzed area in Figure 11b, it is seen that the nucleation density 3×10^{11} agrees well with the experiment. This is also the reason why it was assumed that an appropriate value of the nucleation density is 3×10^{11}.
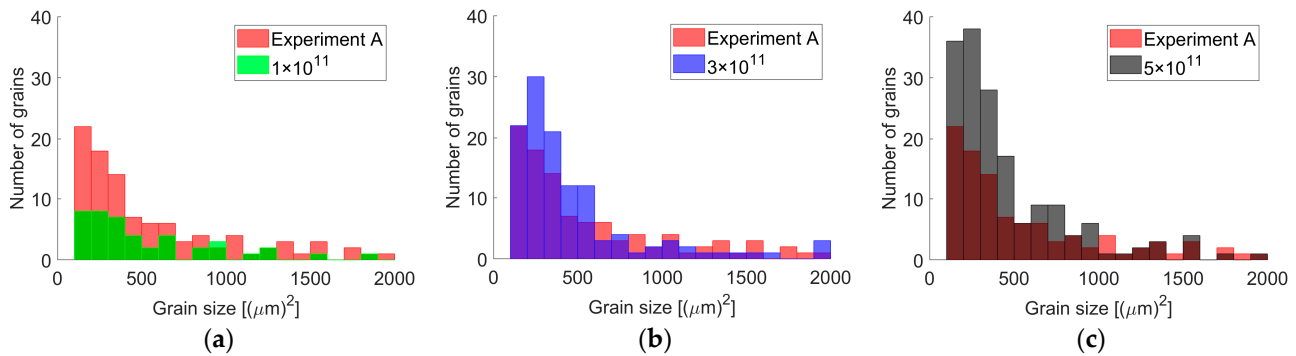

Figure 12. Grain size distribution for different nucleation densities (**a**) 1×10^{11}, (**b**) 3×10^{11}, and (**c**) 5×10^{11} compared with the experimental data adapted from Reference [8].

3.3. Influence on Grain Texture by Changed Process Parameters

As discussed in Section 3.1, the cooling conditions change for the first and last hatch compared to the intermediate hatches. For the second set of parameters only the intermediate zone with hatch numbers 2–8 is analyzed from the simulated grain textures where the cooling conditions are similar. This is referred to as case B with the scan velocity set to 1400 mm/s and the power set to 160 W. The upper 15 μm of the simulation domain is ignored since this zone contains small grains that would disappear if more layers were deposited. This gives a total analyzed area in agreement with the EBSD images in Malmelöv et al. [8]. Figure 13a shows the simulated grain texture for this set of parameters with more pronounced columnar grains compared to case A. Figure 13b shows the aspect ratio for each grain plotted versus its grain size for the simulated grain texture and experimental results, respectively. The general trend of the grain texture is that it contains larger grains compared to case A. Figure 13c shows the number of grains within an interval of grain sizes for case B. The discrepancy between the experimental results in the literature and the simulation can partially be explained by the local variation of the nucleation density in different parts of the build and therefore also the grain texture will vary.
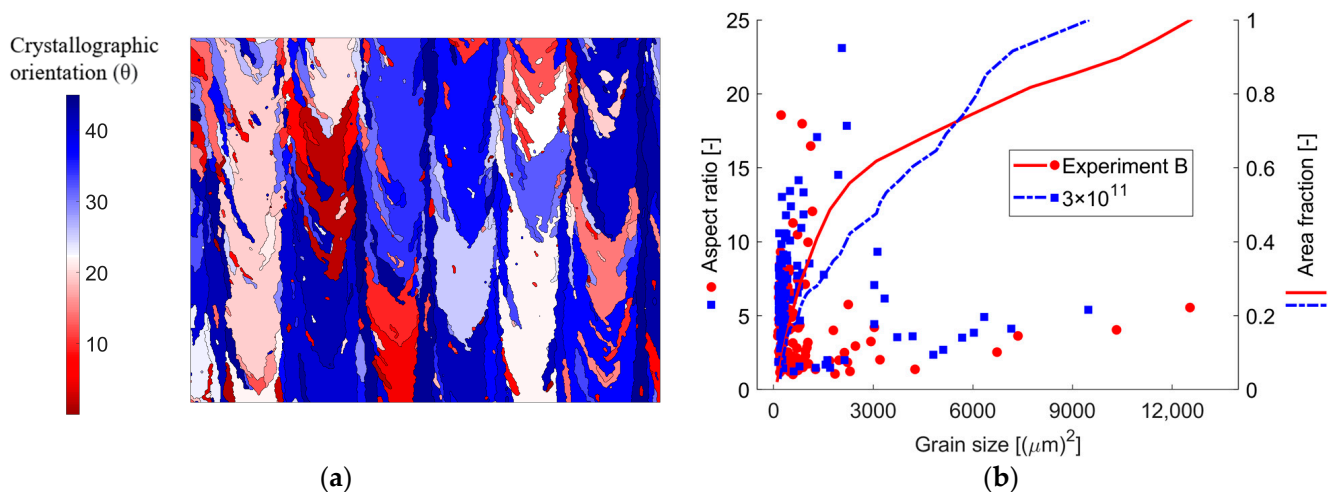

Figure 13. *Cont.*
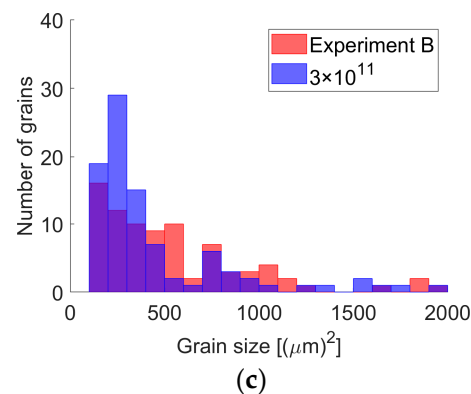
(**c**)

Figure 13. Simulated grain texture (**a**) with nucleation density 3×10^{11} for case B, and comparison between simulation and the adapted experimental data from Reference [8] where (**b**) shows the aspect-ratio vs grain size dot plot and the grains' accumulated contribution to the total analyzed area and (**c**) shows the grain size distribution.

4. Conclusions

A combined finite element and cellular automata model (CA-FE) has been developed to predict the temperature history and grain texture of alloy 625 processed by PBF-LB. The general solidification behavior could be captured using the developed 2D CA-FE model. Epitaxial grain growth can be captured by the 2D CA-FE model, resulting in the columnar grains seen in additive manufactured products. The columnar grains form as coarse grains in the overlap between two adjacent melt pool boundaries, whereas slender elongated grains form in the center of the melt pool. Equiaxed grain growth is also captured by the 2D CA-FE model. The equiaxed grains form when grains nucleated through bulk nucleation suppress the growth of the columnar growth front. The 2D CA-FE model can capture the competitiveness of grain growth where more favorably oriented grains outcompete less favorably oriented grains. The 2D CA-FE model can capture changes in grain texture depending on the process parameters. A higher scan velocity and power resulted in a grain texture with larger grains.

It is seen that the 2D CA-FE model simulates the grain texture which agrees well with the experimental findings in the literature. One essential parameter that has a high influence on the predicted grain texture is the nucleation density. It was shown that comparison to EBSD images can be used to determine suitable nucleation parameters. Although grain growth and nucleation are a 3D phenomenon, a 3D CA-FE model increases the computational time drastically. These computational times are too long for the model to be useful by engineers during process development. It has been shown that the 2D CA-FE model can be used to evaluate the as-printed grain texture depending on the chosen process parameters for PBF-LB such as scan velocity and laser power. The FE simulation runs in about 20 h while the CA model takes about 8 h. The CA computational time could most likely be considerably reduced by parallelization and implementation in a compiled programming language such as Fortran.

Author Contributions: Conceptualization, C.A. and A.L; methodology, C.A. and A.L.; software, C.A.; validation, C.A.; formal analysis, C.A.; investigation, C.A.; resources, A.L.; data curation, C.A.; writing—original draft preparation, C.A. and A.L.; writing—review and editing, C.A. and A.L.; visualization, C.A.; supervision, A.L.; project administration, A.L.; funding acquisition, A.L. All authors have read and agreed to the published version of the manuscript.

Data Availability Statement: The data presented in this study are available on request from the corresponding author.

Conflicts of Interest: The authors declare no conflict of interest.

References

1. Ford, S.; Despeisse, M. Additive Manufacturing and Sustainability: An Exploratory Study of the Advantages and Challenges. *J. Clean. Prod.* **2016**, *137*, 1573–1587. [CrossRef]
2. Petrovic, V.; Gonzalez, J.V.H.; Ferrando, O.J.; Delgado Gordillo, J.; Puchades, J.R.B.; Griñan, L.P. Additive Layered Manufacturing: Sectors of Industrial Application Shown through Case Studies. *Int. J. Prod. Res.* **2011**, *49*, 1061–1079. [CrossRef]
3. Volpato, G.M.; Tetzlaff, U.; Fredel, M.C. A Comprehensive Literature Review on Laser Powder Bed Fusion of Inconel Superalloys. *Addit. Manuf.* **2022**, *55*, 102871. [CrossRef]
4. Dinda, G.P.; Dasgupta, A.K.; Mazumder, J. Laser Aided Direct Metal Deposition of Inconel 625 Superalloy: Microstructural Evolution and Thermal Stability. *Mater. Sci. Eng. A* **2009**, *509*, 98–104. [CrossRef]
5. Shankar, V.; Bhanu Sankara Rao, K.; Mannan, S.L. Microstructure and Mechanical Properties of Inconel 625 Superalloy. *J. Nucl. Mater.* **2001**, *288*, 222–232. [CrossRef]
6. Yan, X.; Gao, S.; Chang, C.; Huang, J.; Khanlari, K.; Dong, D.; Ma, W.; Fenineche, N.; Liao, H.; Liu, M. Effect of Building Directions on the Surface Roughness, Microstructure, and Tribological Properties of Selective Laser Melted Inconel 625. *J. Mater. Process. Technol.* **2021**, *288*, 116878. [CrossRef]
7. Li, C.; White, R.; Fang, X.Y.; Weaver, M.; Guo, Y.B. Microstructure Evolution Characteristics of Inconel 625 Alloy from Selective Laser Melting to Heat Treatment. *Mater. Sci. Eng. A* **2017**, *705*, 20–31. [CrossRef]
8. Malmelöv, A.; Hassila, C.J.; Fisk, M.; Wiklund, U.; Lundbäck, A. Numerical Modeling and Synchrotron Diffraction Measurements of Residual Stresses in Laser Powder Bed Fusion Manufactured Alloy 625. *Mater. Des.* **2022**, *216*, 110548. [CrossRef]
9. Kou, S. *Welding Metallurgy*; Wiley: Hoboken, NJ, USA, 2002.
10. Andreau, O.; Koutiri, I.; Peyre, P.; Penot, J.D.; Saintier, N.; Pessard, E.; De Terris, T.; Dupuy, C.; Baudin, T. Texture Control of 316L Parts by Modulation of the Melt Pool Morphology in Selective Laser Melting. *J. Mater. Process. Technol.* **2019**, *264*, 21–31. [CrossRef]
11. Flood, S.C.; Hunt, J.D. Columnar and Equiaxed Growth: II. Equiaxed Growth Ahead of a Columnar Front. *J. Cryst. Growth* **1987**, *82*, 552–560. [CrossRef]
12. Rappaz, M.; Gandin, C.A. Probabilistic Modelling of Microstructure Formation in Solidification Processes. *Acta Metall. Mater.* **1993**, *41*, 345–360. [CrossRef]
13. Körner, C.; Markl, M.; Koepf, J.A. Modeling and Simulation of Microstructure Evolution for Additive Manufacturing of Metals: A Critical Review. *Metall. Mater. Trans. A* **2020**, *51*, 4970–4983. [CrossRef]
14. Kurz, W.; Rappaz, M.; Trivedi, R. Progress in Modelling Solidification Microstructures in Metals and Alloys. Part II: Dendrites from 2001 to 2018. *Int. Mater. Rev.* **2020**, *66*, 30–76. [CrossRef]
15. Gong, X.; Chou, K. Phase-Field Modeling of Microstructure Evolution in Electron Beam Additive Manufacturing. *JOM* **2015**, *67*, 1176–1182. [CrossRef]
16. Rodgers, T.M.; Madison, J.D.; Tikare, V. Simulation of Metal Additive Manufacturing Microstructures Using Kinetic Monte Carlo. *Comput. Mater. Sci.* **2017**, *135*, 78–89. [CrossRef]
17. Gandin, C.A.; Rappaz, M. A 3D Cellular Automaton Algorithm for the Prediction of Dendritic Grain Growth. *Acta Mater.* **1997**, *45*, 2187–2195. [CrossRef]
18. Gandin, C.A.; Rappaz, M. A Coupled Finite Element-Cellular Automaton Model for the Prediction of Dendritic Grain Structures in Solidification Processes. *Acta Metall. Mater.* **1994**, *42*, 2233–2246. [CrossRef]
19. Dezfoli, A.R.A.; Lo, Y.L.; Raza, M.M. Prediction of Epitaxial Grain Growth in Single-Track Laser Melting of IN718 Using Integrated Finite Element and Cellular Automaton Approach. *Materials* **2021**, *14*, 5202. [CrossRef]
20. Rai, A.; Markl, M.; Körner, C. A Coupled Cellular Automaton–Lattice Boltzmann Model for Grain Structure Simulation during Additive Manufacturing. *Comput. Mater. Sci.* **2016**, *124*, 37–48. [CrossRef]
21. Koepf, J.A.; Soldner, D.; Ramsperger, M.; Mergheim, J.; Markl, M.; Körner, C. Numerical Microstructure Prediction by a Coupled Finite Element Cellular Automaton Model for Selective Electron Beam Melting. *Comput. Mater. Sci.* **2019**, *162*, 148–155. [CrossRef]
22. Teferra, K.; Rowenhorst, D.J. Optimizing the Cellular Automata Finite Element Model for Additive Manufacturing to Simulate Large Microstructures. *Acta Mater.* **2021**, *213*, 116930. [CrossRef]
23. Isoltermics, Nicrofer6020 HMo—Alloy 625. Available online: https://www.isolthermics.com.au/metals/pdfs/common-tech/Alloy%20625%206020hMo.pdf (accessed on 18 August 2023).
24. Special Metals, Inconel Alloy 625. Available online: https://www.specialmetals.com/documents/technical-bulletins/inconel/inconel-alloy-625.pdf (accessed on 18 August 2023).
25. Denlinger, E.R.; Michaleris, P. Effect of Stress Relaxation on Distortion in Additive Manufacturing Process Modeling. *Addit. Manuf.* **2016**, *12*, 51–59. [CrossRef]
26. Wei, L.C.; Ehrlich, L.E.; Powell-Palm, M.J.; Montgomery, C.; Beuth, J.; Malen, J.A. Thermal Conductivity of Metal Powders for Powder Bed Additive Manufacturing. *Addit. Manuf.* **2018**, *21*, 201–208. [CrossRef]

27.   Tinoco, J.; Fredriksson, H. Solidification of a Modified Inconel 625 Alloy under Different Cooling Rates. *High Temp. Mater. Process.* **2004**, *23*, 13–24. [CrossRef]

28.   Goldak, J.; Chakravarti, A.; Bibby, M. A New Finite Element Model for Welding Heat Sources. *Metall. Trans. B* **1984**, *15*, 299–305. [CrossRef]

29.   Lindgren, L.-E. *Computational Welding Mechanics: Thermomechanical and Microstructural Simulations*; Woodhead Publishing Ltd.: Cambridge, UK, 2007; ISBN 9781845692216.

30.   Mohebbi, M.S.; Ploshikhin, V. Implementation of Nucleation in Cellular Automaton Simulation of Microstructural Evolution during Additive Manufacturing of Al Alloys. *Addit. Manuf.* **2020**, *36*, 101726. [CrossRef]

31.   Lipton, J.; Glicksman, M.E.; Kurz, W. Dendritic Growth into Undercooled Alloy Metals. *Mater. Sci. Eng.* **1984**, *65*, 57–63. [CrossRef]

32.   Kurz, W.; Giovanola, B.; Trivedi, R. Theory of Microstructural Development during Rapid Solidification. *Acta Metall.* **1986**, *34*, 823–830. [CrossRef]

33.   Zinoviev, A.; Zinovieva, O.; Ploshikhin, V.; Romanova, V.; Balokhonov, R. Evolution of Grain Structure during Laser Additive Manufacturing. Simulation by a Cellular Automata Method. *Mater. Des.* **2016**, *106*, 321–329. [CrossRef]

34.   Tsai, D.C.; Hwang, W.S. A Three Dimensional Cellular Automaton Model for the Prediction of Solidification Morphologies of Brass Alloy by Horizontal Continuous Casting and Its Experimental Verification. *Mater. Trans.* **2011**, *52*, 787–794. [CrossRef]

35.   Wang, W.; Lee, P.D.; McLean, M. A Model of Solidification Microstructures in Nickel-Based Superalloys: Predicting Primary Dendrite Spacing Selection. *Acta Mater.* **2003**, *51*, 2971–2987. [CrossRef]

36.   Yang, M.; Wang, L.; Yan, W. Phase-Field Modeling of Grain Evolutions in Additive Manufacturing from Nucleation, Growth, to Coarsening. *NPJ Comput. Mater.* **2021**, *7*, 56. [CrossRef]

37.   Wang, L.Y.; Wang, Y.C.; Zhou, Z.J.; Wan, H.Y.; Li, C.P.; Chen, G.F.; Zhang, G.P. Small Punch Creep Performance of Heterogeneous Microstructure Dominated Inconel 718 Fabricated by Selective Laser Melting. *Mater. Des.* **2020**, *195*, 109042. [CrossRef]